J. Fluid Mech. (2020), *vol.* 889, A29. © The Author(s), 2020.
Published by Cambridge University Press
doi:10.1017/jfm.2020.100

Uncovering Townsend's wall-attached eddies in low-Reynolds-number wall turbulence

Cheng Cheng[1], Weipeng Li[1,†], Adrián Lozano-Durán[2] and Hong Liu[1]

[1]School of Aeronautics and Astronautics, Shanghai Jiao Tong University, Shanghai 200240, PR China
[2]Center for Turbulence Research, Stanford University, CA 94305, USA

(Received 25 July 2019; revised 15 January 2020; accepted 30 January 2020)

A growing body of studies supports the existence of Townsend's wall-attached eddies in wall turbulence under the condition of sufficiently high Reynolds numbers. In the present work, we uncover the signature of Townsend's wall-attached eddies in low-Reynolds-number wall turbulence. To this end, we use a three-dimensional clustering methodology to identify the wall-attached structures of intense streamwise and spanwise velocity fluctuations in turbulent channel flows at four Reynolds numbers ($Re_\tau = 186$, 358, 547 and 934). The statistical properties of the structures, such as their geometric self-similarity, population density and statistical moments, are investigated and compared with the predictions of the attached-eddy model. Particular attention is paid to the asymmetries between high- and low-speed wall-attached streaky structures, and we show that the former are a closer representation of the wall-attached eddies. This observation is ascribed to the differences between the sweep and ejection events associated with the streaks. We also examine the Reynolds-number effects on the statistical properties of the structures, and find that the signature of attached eddies can be observed within the Reynolds-number range under scrutiny. Our approach paves the way to cost-efficient model development and flow prediction using computationally more affordable simulations at low Reynolds numbers.

Key words: boundary layer structure, turbulent boundary layers

1. Introduction

In the 1970s, Townsend (1976) proposed a conceptual model describing the multi-scale nature of fluid motions in wall-bounded turbulence. He conjectured that the logarithmic region of wall turbulence is populated by a collection of randomly distributed momentum-carrying motions (or eddies) with their roots attached to the 'wall' (the near-wall region). Townsend (1976) further hypothesised that the population density of the eddies decays proportionally to the distance to the wall (y), and that their sizes scaled with y. The model was extended by Perry and co-authors (Perry & Chong 1982; Perry, Henbest & Chong 1986; Perry & Marusic 1995) and has been recently reviewed by Marusic & Monty (2019). A growing number of studies have supported the existence of the attached eddies in wall-bounded turbulence

† Email address for correspondence: liweipeng@sjtu.edu.cn

(e.g. Lozano-Durán, Flores & Jiménez 2012; Hwang 2015; Hellström, Marusic & Smits 2016; Hwang & Bengana 2016; Baars, Hutchins & Marusic 2017; Hwang & Sung 2018, 2019; Cheng *et al.* 2019; Yang, Willis & Hwang 2019; Baars & Marusic 2020; Hu, Yang & Zheng 2020) or complemented the original picture by Townsend (Davidson, Nickels & Krogstad 2006; Mizuno & Jiménez 2011; Dong *et al.* 2017; Mouri 2017; Lozano-Durán & Bae 2019).

Under the attached-eddy model framework, the turbulence intensities can be predicted as

$$\langle u^{+2}\rangle = -A_1 \ln(y/h) + B_1, \tag{1.1a}$$

$$\langle w^{+2}\rangle = -C_1 \ln(y/h) + D_1, \tag{1.1b}$$

$$\langle v^{+2}\rangle = E_1, \tag{1.1c}$$

where u, w and v are the streamwise, spanwise and wall-normal velocity fluctuations, respectively, h is the boundary-layer thickness (or channel half-height) and A_1, B_1, C_1, D_1 and E_1 are constants. The superscript $+$ denotes normalisation in wall units. By assuming that the probability density function (p.d.f.) of u is Gaussian, Meneveau & Marusic (2013) extended (1.1*a*) to high-order moments and showed that a similar logarithmic scaling holds for the $2p$th moment

$$\langle u^{+2p}\rangle^{1/p} = -A_p \ln(y/h) + B_p. \tag{1.2}$$

Yang *et al.* (2018) and Mehrez *et al.* (2019) found that the $2p$th moment of w also follows the logarithmic scaling according to the attached-eddy model

$$\langle w^{+2p}\rangle^{1/p} = -C_p \ln(y/h) + D_p. \tag{1.3}$$

The constants A_p, B_p, C_p and D_p depend on the number p.

The logarithmic decay of the statistical moments with respect to y is considered to be one of the most compelling indicators in favour of the attached-eddy model, and its validity has been assessed in numerous studies by Hultmark *et al.* (2012), Marusic *et al.* (2013), Meneveau & Marusic (2013), Sillero, Jiménez & Moser (2013), Lee & Moser (2015), Hu & Zheng (2018) and Yamamoto & Tsuji (2018), among others. Hultmark *et al.* (2012) tested the scaling in (1.1*a*) by measuring turbulent pipe flows at $Re_\tau \geqslant 20\,000$. Yamamoto & Tsuji (2018) reported the logarithmic variations of the streamwise velocity fluctuations in the direct numerical simulation (DNS) of turbulent channel flows up to $Re_\tau = 8000$. Meneveau & Marusic (2013) found that high-order moments obey (1.2), from $2p = 4$ to $2p = 10$, in turbulent boundary layers at $Re_\tau > 7300$. However, the logarithmic decay of $\langle u^{+2p}\rangle^{1/p}$ has been only observed at high Reynolds numbers, $Re_\tau \sim O(10^4)$, and it is practically non-existent otherwise. For w, the scaling in (1.1*b*) has been observed at a much lower Reynolds number compared to that of u (Jiménez & Hoyas 2008; Sillero *et al.* 2013; Lee & Moser 2015). Very recently, Mehrez *et al.* (2019) reported that the logarithmic scaling in (1.3) holds in turbulent channel flows from $Re_\tau = 1000$ to $Re_\tau = 4000$.

In the present work, we aim to answer the question: can Townsend's wall-attached eddies be identified in low-Reynolds-number wall turbulence? If yes, this would imply that the characteristics of the wall-attached eddies could be evaluated at a lower computational and experimental cost than the numerical set-ups and experiments discussed above. Many techniques for identifying attached eddies lie on the separation of the multi-scale energetic motions in the flow. Among them, cutoff spectral filters

(Mathis *et al.* 2013; Chung *et al.* 2015; Hwang & Sung 2017) and adaptive mode decomposition (AMD) (Agostini & Leschziner 2014, 2019; Wang, Pan & Wang 2018, 2019; Cheng *et al.* 2019) emerge as attractive candidates to extract multi-scale attached eddies. However, cutoff spectral filters suffer from artificial selection of thresholds (Wang *et al.* 2018), and AMD is incapable of capturing smooth scale variations in the logarithmic region (Cheng *et al.* 2019; Agostini & Leschziner 2019).

Alternatively, the identification of flow structures based on the three-dimensional clustering of a region where a quantity of interest is intense has proven effective in elucidating eddies at multiple scales (Del Álamo *et al.* 2006; Lozano-Durán *et al.* 2012). The method has been successfully employed to investigate multi-scale vortex packets (Del Álamo *et al.* 2006) and the structures responsible for intense momentum transfer in turbulent channel flows (Lozano-Durán *et al.* 2012; Lozano-Durán & Jiménez 2014). Recently, Hwang & Sung (2018) adopted the same methodology to analyse the wall-attached structures of intense velocity fluctuations in a turbulent boundary layer at $Re_\tau = 980$. They examined the second-order moments carried by the structures, and concluded that the identified structures underpin Townsend's attached eddies. In their further work (Hwang & Sung 2019), they reported that high-speed u-structures identified in turbulent pipe flows at $Re_\tau = 930$ and 3008 obey the logarithmic scaling with respect to y, but the same behaviour is not observed for the low-speed streaks. The asymmetry was ascribed to the differences of the local Reynolds number in the logarithmic layer.

To date, the studies on wall-attached eddies have mostly focused on turbulent flows at moderate and high Reynolds numbers, i.e. $Re_\tau \gtrsim 1000$ (Del Álamo *et al.* 2006; Lozano-Durán *et al.* 2012; Lozano-Durán & Jiménez 2014; Hwang 2015; Lozano-Durán & Borrell 2016; Baars *et al.* 2017; Hwang & Sung 2018, 2019; Deshpande, Monty & Marusic 2019; Hu *et al.* 2020). In the present work, we intend to uncover the signature of Townsend's wall-attached eddies in low-Reynolds-number wall turbulence and examine their scale-based properties in detail. We will pay special attention to the asymmetries between high- and low-speed wall-attached structures, as an increasing body of studies has reported that this asymmetric behaviour is an inherent characteristic of the velocity fluctuations. For example, Agostini & Leschziner (2016*a*,*b*, 2019) stated that the modulation of the near-wall streamwise velocity fluctuations by outer large-scale motions is exceedingly asymmetric. The amplification caused by positive outer large-scale motions is much stronger than the attenuation from negative ones. Therefore, the sign of the structures is an indispensable factor for the identification and investigation of the flow structure. Additionally, the assessment of logarithmic scaling laws for the high-order moments carried by the wall-attached structures can provide further physical support in favour of the attached-eddy model, which is another topic of interest in the present study.

This paper is organised as follows. In § 2, we introduce the DNS database and structure identification method adopted in the present study. We then show the geometrical characteristics and high-order moments of the identified structures in § 3. In this section we also provide an interpretation of the asymmetric behaviour between high- and low-speed wall-attached u-structures. Concluding remarks are summarised in § 4.

2. DNS database and structure identification method

The DNS database used in the present study has been extensively validated by Jiménez and co-workers (Del Álamo *et al.* 2004; Hoyas & Jiménez 2006; Lozano-Durán *et al.* 2012; Lozano-Durán & Jiménez 2014). Four cases at $Re_\tau = 186$, 358,

Case	Re_τ	$L_x(h)$	$L_y(h)$	$L_z(h)$	Δx^+	Δz^+	Δy^+_{min}	Δy^+_{max}	N_F
Re180	186	12π	2	4π	9.1	4.6	0.1	5.9	106
Re350	358	8π	2	3π	8.8	4.3	0.05	5.8	21
Re550	547	8π	2	4π	13.4	6.8	0.04	6.7	142
Re950	934	8π	2	3π	11.5	5.7	0.03	7.6	73

TABLE 1. Parameter settings in the DNSs. Here, L_x, L_y and L_z are the sizes of the computational domains in the streamwise, wall-normal and spanwise direction, respectively. Δx^+ and Δz^+ denote the streamwise and spanwise grid resolutions in inner units, respectively. Δy^+_{min} and Δy^+_{max} are the finest and coarsest resolutions in the wall-normal direction, respectively. N_F is the number of flow fields adopted to accumulate statistics.

547 and 934 are chosen, and named Re180, Re350, Re550 and Re950, respectively. Details of the parameter settings are listed in table 1. Hereafter, x, y and z stand for the streamwise, wall-normal and spanwise directions, respectively.

We adopt a clustering methodology (Moisy & Jiménez 2004; Del Álamo *et al.* 2006; Lozano-Durán *et al.* 2012; Lozano-Durán & Jiménez 2014; Dong *et al.* 2017; Osawa & Jiménez 2018; Hwang & Sung 2018, 2019; Yoon *et al.* 2020) to identify three-dimensional structures of intense velocity fluctuations (u and w) populating the channel. The structures are defined as spatially connected regions satisfying

$$\phi(x, y, z) > \alpha\phi_{rms}(y), \tag{2.1}$$

and

$$\phi(x, y, z) < -\alpha\phi_{rms}(y), \tag{2.2}$$

which are termed positive (high-speed) and negative (low-speed) structures, respectively, where ϕ represents either streamwise or spanwise velocity fluctuations (u or w), ϕ_{rms} denotes the root-mean-square of ϕ and α is a positive threshold value. The value of α is set equal to 1.5 based on the percolation theory (Moisy & Jiménez 2004; Lozano-Durán *et al.* 2012; Hwang & Sung 2018). We have tested that the results in the present study are qualitatively similar for α in the range of $1.3 \leqslant \alpha \leqslant 1.7$ (see appendix A).

Geometrically, the structures identified by (2.1) and (2.2) are characterised by l^+_x, l^+_y, l^+_z and y^+_{min}, where l^+_x, l^+_y and l^+_z denote the length, height and width, respectively, of the bounding boxes of each structure when aligned with the mean-flow direction, and y^+_{min} is the minimum distance of the structure to the wall. Under the condition $y^+_{min} < 1$, the structures are classified into two families: wall-attached structures if $y^+_{min} < 1$, and detached structures otherwise. Accordingly, the structures are labelled as positive wall attached (*PA*), positive wall detached (*PD*), negative wall attached (*NA*) and negative wall detached (*ND*). We further used the subscripts u and w to distinguish the structures identified by using different velocity fluctuations.

Tables 2–5 summarise the number (N), number fraction (N/N_m), volume fraction (V/V_m) and energy fractions (E/E_m, E/E_t) of u- and w-structures for all cases, where $V = \sum(l_x l_y l_z)$, $E = \sum \frac{1}{2}\phi^2$ and the sum is applied to different families (*PA*, *PD*, *NA* or *ND*). The total quantities computed over all identified structures and over the whole channel are denoted by the subscripts m and t, respectively. The results from tables 2–5 show that the number of attached structures is smaller than the detached ones, but their volume and energy are notably larger. The energy of

	N	N/N_m	V/V_m	E/E_m	E/E_t
PA_u	40 756	0.2434	0.3362	0.3082	0.1456
PD_u	47 969	0.2865	0.0486	0.0369	0.0174
NA_u	17 065	0.1019	0.5565	0.5656	0.2671
ND_u	61 641	0.3682	0.0587	0.0892	0.0421
PA_w	52 593	0.1728	0.4055	0.3729	0.1994
PD_w	99 896	0.3281	0.0934	0.1254	0.0671
NA_w	52 289	0.1718	0.4062	0.3743	0.2001
ND_w	99 649	0.3273	0.0949	0.1274	0.0681

TABLE 2. The number (N), number fraction (N/N_m), volume fraction (V/V_m) and energy fractions (E/E_m, E/E_t) of the identified u- and w-structures in Re180.

	N	N/N_m	V/V_m	E/E_m	E/E_t
PA_u	13 898	0.2067	0.4005	0.3511	0.1710
PD_u	20 344	0.3025	0.0383	0.0355	0.0173
NA_u	6 461	0.0960	0.5194	0.5418	0.2639
ND_u	26 550	0.3948	0.0417	0.0716	0.0349
PA_w	18 404	0.1521	0.4001	0.3789	0.2016
PD_w	42 305	0.3496	0.0953	0.1177	0.0626
NA_w	18 405	0.1521	0.4168	0.3902	0.2076
ND_w	41 907	0.3463	0.0879	0.1132	0.0602

TABLE 3. The number (N), number fraction (N/N_m), volume fraction (V/V_m) and energy fractions (E/E_m, E/E_t) of the identified u- and w-structures in Re350.

	N	N/N_m	V/V_m	E/E_m	E/E_t
PA_u	275 962	0.1956	0.4076	0.3754	0.1691
PD_u	433 330	0.3072	0.0374	0.0355	0.0151
NA_u	125 423	0.0889	0.5200	0.5280	0.2379
ND_u	575 897	0.4083	0.0350	0.0631	0.0284
PA_w	338 977	0.1354	0.4320	0.3964	0.1982
PD_w	908 925	0.3631	0.0752	0.1061	0.0531
NA_w	340 696	0.1361	0.4166	0.3906	0.1953
ND_w	914 805	0.3654	0.0762	0.1069	0.0535

TABLE 4. The number (N), number fraction (N/N_m), volume fraction (V/V_m) and energy fractions (E/E_m, E/E_t) of the identified u- and w-structures in Re550.

attached structures (*PA* and *NA*) accounts for nearly 40 % of E_t, whereas the energy of detached structures (*PD* and *ND*) accounts only for 1 %–5 %. The difference suggests that wall-attached structures are representative of the energy-containing motions in turbulent flows. Consequently, in the following sections, we focus on *PA* and *NA* and their relationship with the predictions of the attached-eddy model.

3. Results and discussion

The statistical properties of the wall-attached u- and w-structures are analysed separately in §§ 3.1 and 3.2 by using Re550. The other three cases (Re180, Re350 and Re950) are included in § 3.3 to access the Reynolds-number effects on the

	N	N/N_m	V/V_m	E/E_m	E/E_t
PA_u	269 695	0.1634	0.4621	0.4138	0.2060
PD_u	535 122	0.3243	0.0328	0.0269	0.0134
NA_u	116 439	0.0706	0.4751	0.5101	0.2540
ND_u	728 883	0.4417	0.0301	0.0493	0.0245
PA_w	332 340	0.1120	0.4225	0.4075	0.2189
PD_w	1150 654	0.3878	0.0748	0.0927	0.0498
NA_w	332 504	0.1121	0.4260	0.4066	0.2184
ND_w	1151 862	0.3882	0.0767	0.0932	0.0501

TABLE 5. The number (N), number fraction (N/N_m), volume fraction (V/V_m) and energy fractions (E/E_m, E/E_t) of the identified u- and w-structures in Re950.

statistical properties of the structures. Bearing in mind the three key features of Townsend's attached eddies: (i) their sizes are proportional to y, (ii) their population density is inversely proportional to y and (iii) the statistical moments of the inactive parts (u and w) follow logarithmic wall-normal scalings, we examine the properties of the structures from each of these perspectives.

3.1. *The wall-attached u-structures*

3.1.1. *Length-scale self-similarity*

The geometrical properties of the wall-attached u-structures (PA_u and NA_u) in Re550 are examined by the joint p.d.f.s of l_x^+, l_z^+ with respect to l_y^+, as shown in figure 1. Hereafter, we mainly focus on the large-scale structures, i.e. those with $l_y^+ > 100$, whose wall-normal centres are approximately located at $y^+ > 50$. It can be seen that l_x^+ and l_z^+ increase with l_y^+ according to well-defined scaling laws. Nonlinear relationships are observed between l_x^+ and l_y^+, that is $l_x^+ \propto (l_y^+)^{0.70}$ for PA_u and $l_x^+ \propto (l_y^+)^{0.88}$ for NA_u, and a linear relationship is well exhibited between l_z^+ and l_y^+. These sizes are approximately consistent with the observations in a turbulent boundary layer (Hwang & Sung 2018), suggesting that the geometrical self-similarity of spanwise length scales is also present in the wall turbulence even at much lower Reynolds numbers.

We next analyse the wall-normal decay of the population density of structures. Following Lozano-Durán *et al.* (2012), we define the population density as $n_d(l_y^+) = N_i(l_y^+)/(2N_F A)$, where $N_i(l_y^+)$ is the number of structures with a given l_y^+, N_F is number of the flow fields and A represents the area of the wall $L_x \times L_z$. Figure 2 displays n_d as a function of l_y^+. The density of structures decays as $n_d \propto (l_y^+)^{-1.9}$ for NA_u, while for PA_u the density is well approximated by $n_d \propto (l_y^+)^{-1.3}$. Since the expected theoretical estimation of n_d obeys $n_d \propto (l_y^+)^{-1}$ (Perry & Chong 1982; Perry *et al.* 1986), the population density of PA_u follows more closely the prediction of the attached-eddy theory than that of NA_u.

3.1.2. *Logarithmic wall-normal scaling of the statistical moments*

To evaluate the scaling of the statistical moments and further examine the differences between PA_u and NA_u, we define the conditional statistical moment of u as

$$\langle u_a^{2p+}\rangle^{1/p}(y, l_y^+) = \left\{ \frac{1}{N_u(y, l_y^+)} \sum_{i=1}^{N_u(y,l_y^+)} \left[\frac{u_i(x, y, z)|_{l_y^+}}{u_\tau} \right]^{2p} \right\}^{1/p}, \tag{3.1}$$

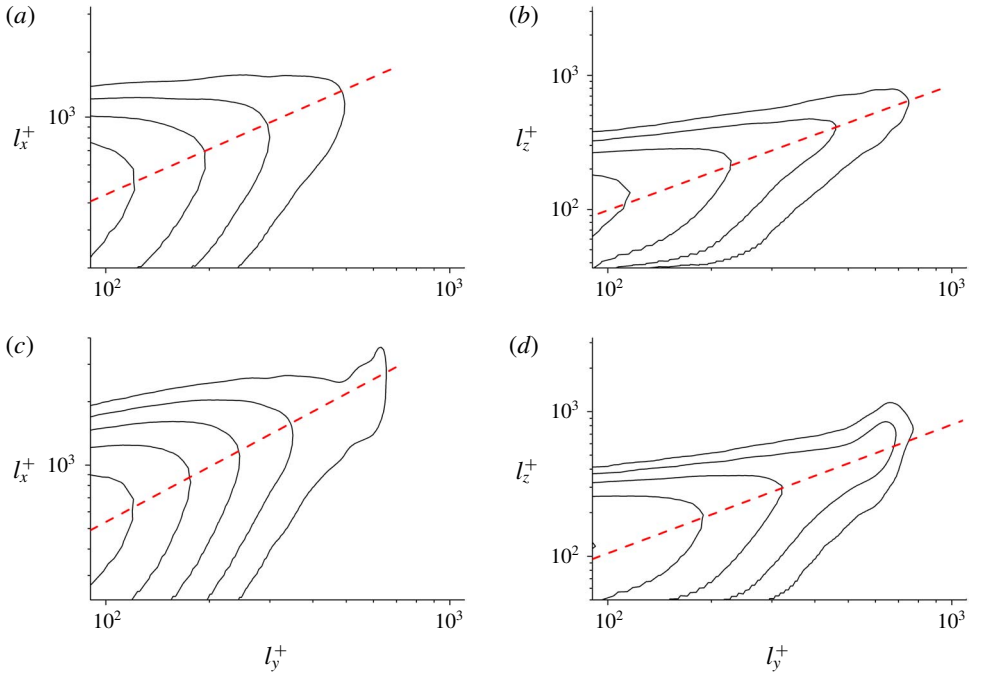

FIGURE 1. (*a*,*b*) Joint p.d.f.s of the length (l_x^+) and width (l_z^+) of PA_u in Re550 with respect to their height (l_y^+). The red dashed lines in (*a*,*b*) denote $l_x^+ = 17.41(l_y^+)^{0.70}$ and $l_z^+ = l_y^+$, respectively. (*c*,*d*) Joint p.d.f.s of the length (l_x^+) and width (l_z^+) of NA_u in Re550 with respect to their height (l_y^+). The red dashed lines in (*c*,*d*) denote $l_x^+ = 9.88(l_y^+)^{0.88}$ and $l_z^+ = l_y^+$, respectively. All of these p.d.f.s are logarithmically distributed.

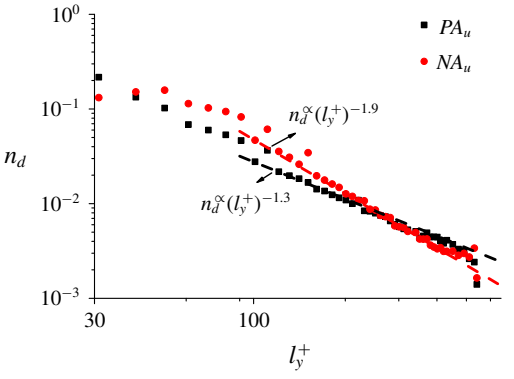

FIGURE 2. The population density (n_d) of PA_u and NA_u as a function of l_y^+ in Re550. The red and black dashed lines represent $n_d \propto (l_y^+)^{-1.9}$ and $n_d \propto (l_y^+)^{-1.3}$, respectively.

where $N_u(y, l_y^+)$ denotes the number of grid points belonging to a structure with l_y^+ at a given y, and $u_i(x, y, z)|_{l_y^+}$ denotes the streamwise velocity fluctuation of the ith grid point of the structure. In this manner, $\langle u_a^{2p+} \rangle^{1/p}$ represents the $2p$th root of the streamwise velocity moment carried by the structures with a given scale l_y^+.

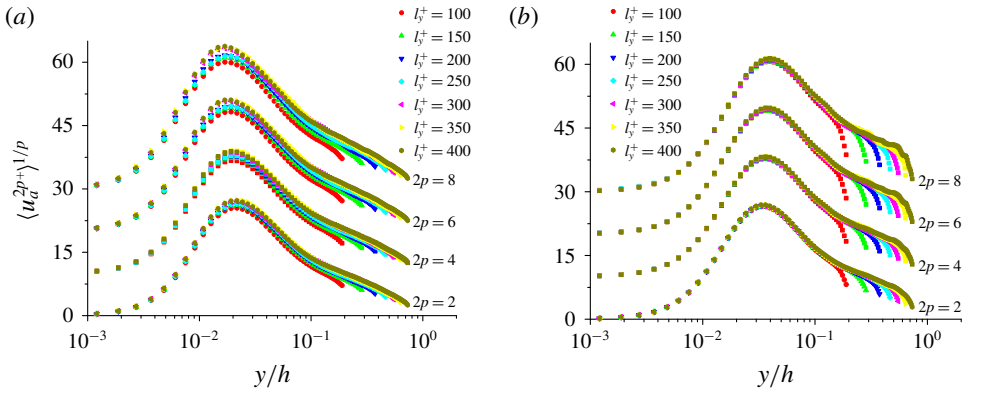

FIGURE 3. Wall-normal variations of the $2p$th root of moments of the streamwise velocity fluctuations carried by PA_u (*a*) and NA_u (*b*) with several selected wall-normal heights in Re550. The profiles of the 4th, 6th and 8th roots of the moments are shifted upward by $\Delta\langle u_a^{4+}\rangle^{1/2} = 10$, $\Delta\langle u_a^{6+}\rangle^{1/3} = 20$ and $\Delta\langle u_a^{8+}\rangle^{1/4} = 30$, respectively.

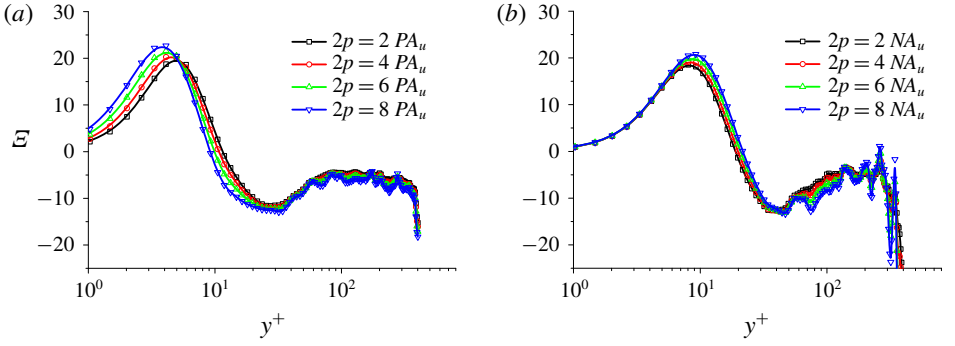

FIGURE 4. Wall-normal variations of the corresponding indicator functions of the statistical moments from $2p = 2$ to $2p = 8$ for PA_u (*a*) and NA_u (*b*) with $l_y^+ = 400$ in Re550.

Figure 3 shows the profiles of $\langle u_a^{2p+}\rangle^{1/p}$, from $2p = 2$ to $2p = 8$, carried by structures with several selected l_y^+ in Re550. The figure reveals that, for increasing l_y^+, the profiles tend to decay logarithmically. To quantify the logarithmic decay in a systematic manner, we define the indicator function $\Xi = y(\partial\langle u_a^{2p+}\rangle^{1/p}/\partial y)$. Figure 4 shows the value of Ξ as a function of y^+, for the structures with $l_y^+ = 400$. Comparatively well-defined plateaus are observed for PA_u regardless of the value of p. On the contrary, Ξ does not approach a constant value for NA_u. This phenomenon, together with the observations in § 3.1.1, suggests that PA_u are more inclined to behave akin to ideal wall-attached eddies.

3.1.3. *Inner peaks of the statistical moments of the streamwise velocity fluctuation*

Another consequence of the attached-eddy model is the increase of the inner peaks of the second-order moment of u as $\ln(Re_\tau)$, which has been validated in previous numerical and experimental studies (Marusic & Kunkel 2003; Hoyas & Jiménez 2006; Lee & Moser 2015; Marusic, Baars & Hutchins 2017). By assuming that the inner

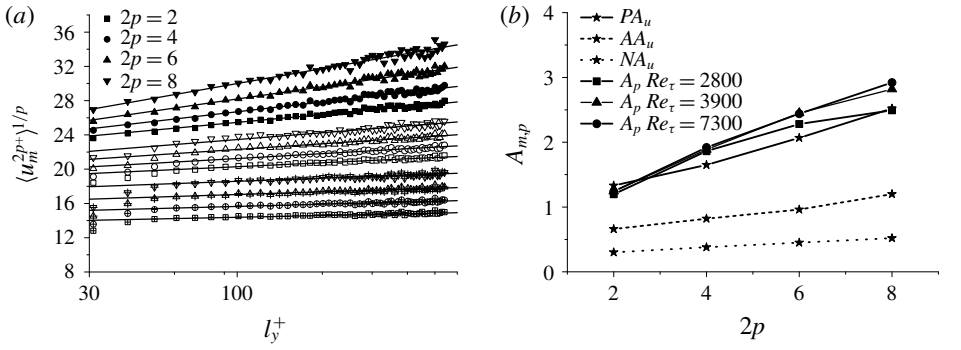

FIGURE 5. (*a*) Variations of inner peaks ($\langle u_m^{2p+}\rangle^{1/p}$) as a function of l_y^+ in Re550. The solid symbols denote PA_u, hollow symbols denote AA_u and hollow symbols with '+' denote NA_u. The symbols of AA_u and NA_u are shifted downward by $\Delta\langle u_m^{2p+}\rangle^{1/p} = 5$ and $\Delta\langle u_m^{2p+}\rangle^{1/p} = 12$, respectively. The solid lines are the fitting curves. (*b*) Variations of the growth rates of the inner peaks ($A_{m,p}$) as a function of the moment order $2p$ in Re550, compared with the A_p obtained from experiments (Meneveau & Marusic 2013).

peaks are the sole outcome of the wall-attached eddies residing in the logarithmic region, Meneveau & Marusic (2013) derived a generalised formula for the inner peaks of the statistical moments of u,

$$\langle u_m^{2p+}\rangle^{1/p} \sim A_p \ln Re_\tau, \tag{3.2}$$

where the coefficients A_p are identical to those in (1.2), and represent the growth rates of the inner peaks.

Considering that l_y^+ can be interpreted as local Re_τ, by using the case of Re550, we further show in figure 5(*a*) the variations of $\langle u_m^{2p+}\rangle^{1/p}$ as a function of l_y^+. For comparison, the wall-attached u-structures satisfying both (2.1) and (2.2), are also included and named AA_u, where $AA_u = PA_u + NA_u$. The inner peaks increase logarithmically with l_y^+ both for the high- and low-speed wall-attached u-structures, although the associated growth rates are different. In figure 5(*b*), the growth rates are compared with the high-Reynolds-number experimental results by Meneveau & Marusic (2013). The growth rates of PA_u are approximately in agreement with the experimental data, while the growth rates of AA_u are approximately half of those of PA_u due to the relatively smaller values of NA_u.

Recalling that both in experimental measurements and simulations the growth rates of the inner peaks are found to be lower than the theoretical predictions of A_p in (3.2), an empirical factor $(1-\gamma)$ was introduced to correct A_p with $\gamma = 0.5$ (Klewicki, Fife & Wei 2009; Alfredsson, Segalini & Örlü 2011; Meneveau & Marusic 2013; Marusic *et al.* 2017). Note that, in these studies, no high- and low-speed scale separation has been conducted, similar to AA_u in the present study. The results from figure 5 suggest that, although the features of the inner peaks of AA_u are consistent with the experimental results for the empirical correction on A_p, the positive structures are again more in line with the theoretical predictions of the attached-eddy model.

3.1.4. *An interpretation of the asymmetric behaviour between PA_u and NA_u*

The comparison of PA_u and NA_u has shown that the former follow more closely the theoretical predictions of the attached-eddy model framework. Hwang & Sung (2019)

observed a similar behaviour for the scale-based streamwise velocities in turbulent pipe flows up to $Re_\tau = 3008$. In their work, they attributed this phenomenon to the differences in the local Re_τ conditioned to the presence of high- and low-speed streaks. In that respect, high-speed streaks are locally associated with higher Reynolds numbers, which was used to justify the emergence of logarithmic trends in quantities conditioned to the aforementioned structures. However, a similar analysis using our data (Re550) indicates that the friction Reynolds number conditioned to the presence of high-speed streaks is at most $Re_\tau \approx 1000$, which is still too low to explain the appearance of the logarithmic trends in PA_u discussed in previous subsections. Therefore, our results suggest that the differences in the local Reynolds number are probably not essential to understand the asymmetries between NA_u and PA_u reported above.

We provide an alternative interpretation of the differences between PA_u and NA_u based on the asymmetries of the fluid advected by sweeps and ejections. We measure u and v within the interior region of an identified structure to examine the averaged advection of the structure from the perspective of the quadrant decomposition (Wallace 2016). For the wall-attached u-structures (PA_u and NA_u) with $l_y^+ = 400$, the joint p.d.f.s of u^+ and v^+ at $y/h = 0.1$ and $y/h = 0.2$ are displayed in figure 6. The results reveal that PA_u with $l_y^+ = 400$ are associated with sweep events ($u^+ > 0$, $v^+ < 0$), while NA_u with $l_y^+ = 400$ are strongly correlated with the ejection events ($u^+ < 0$, $v^+ > 0$). This observation holds for varying l_y^+.

Consequently, PA_u are predominantly dominated by low shear flow from the upper region of the boundary layer, while NA_u are strongly influenced by the higher shear and turbulence intensities of the near-wall region. The difference can be quantified more precisely using the Corrsin shear parameter (Corrsin 1958) $S^* = SL_\varepsilon/q$, which not only characterises the strength of the mean shear S, controlling the dynamics of eddies with integral length scale L_ε and turbulent kinetic energy q^2, but also stands for the ratio of the equilibration time L_ε/q (denoted as ET hereafter) and the life time $1/S$ (denoted as LT hereafter) of the eddies (Jiménez 2018).

To shed light on the difference in the mean shear between PA_u and NA_u, we define the conditional (scale-based) mean streamwise velocity, turbulent kinetic energy and dissipation as

$$\langle U_a\rangle(y, l_y^+) = \left\{ \frac{1}{N_u(y, l_y^+)} \sum_{i=1}^{N_u(y,l_y^+)} U_i(x, y, z)|_{l_y^+} \right\}, \tag{3.3}$$

$$\langle q_a^2\rangle(y, l_y^+) = \left\{ \frac{1}{N_u(y, l_y^+)} \sum_{i=1}^{N_u(y,l_y^+)} q_i^2(x, y, z)|_{l_y^+} \right\}, \tag{3.4}$$

$$\langle \epsilon_a\rangle(y, l_y^+) = \left\{ \frac{1}{N_u(y, l_y^+)} \sum_{i=1}^{N_u(y,l_y^+)} \epsilon_i(x, y, z)|_{l_y^+} \right\}, \tag{3.5}$$

respectively, where $U_i(x, y, z)|_{l_y^+}$, $q_i^2(x, y, z)|_{l_y^+}$ and $\epsilon_i(x, y, z)|_{l_y^+}$ denote instantaneous streamwise velocity, turbulent kinetic energy and dissipation of the ith grid point of the structure with size l_y^+, respectively. The mean shear is calculated by $S_a(y)|_{l_y^+} = \partial\langle U_a\rangle/\partial y|_{l_y^+}$, and the conditional shear parameter is expressed as

$$S_a^*(y) = \frac{S_a\langle q_a^2\rangle}{\langle \epsilon_a\rangle}. \tag{3.6}$$

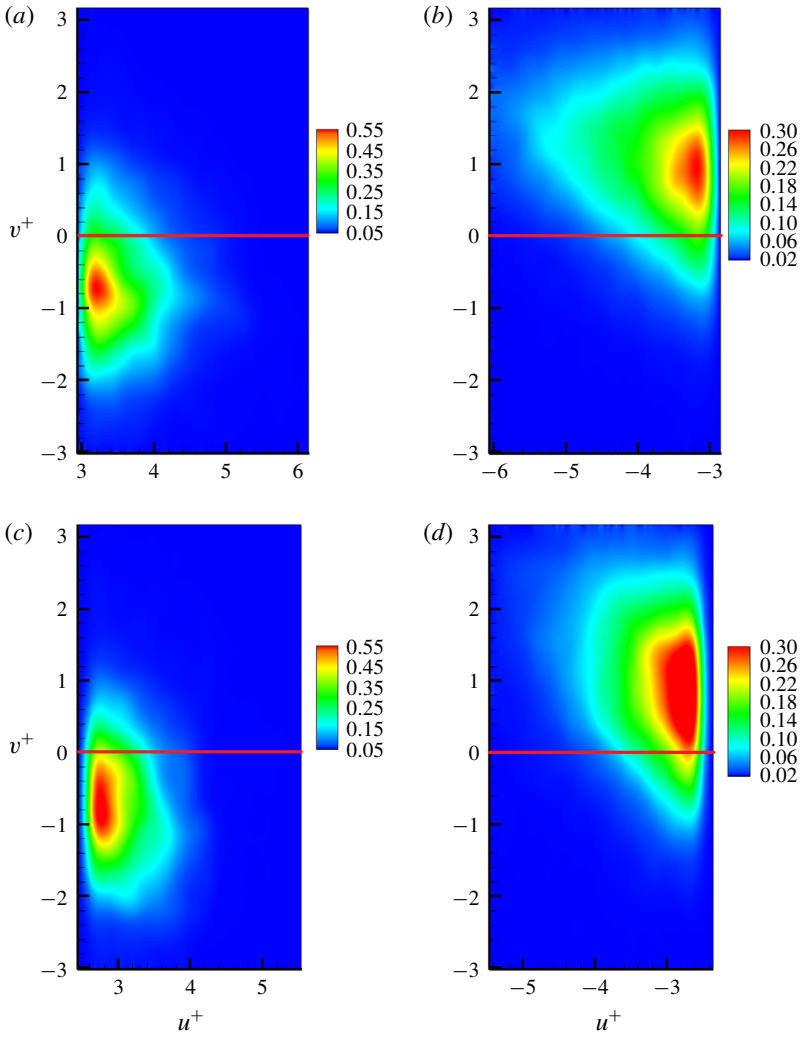

FIGURE 6. (*a*,*b*) The joint p.d.f.s of u^+ and v^+ at $y/h = 0.1$ for PA_u (*a*) and NA_u (*b*) with $l_y^+ = 400$ in Re550. (*c*,*d*) The joint p.d.f.s of u^+ and v^+ at $y/h = 0.2$ for PA_u (*c*) and NA_u (*d*) with $l_y^+ = 400$ in Re550. The red lines denote $v^+ = 0$.

Figure 7(*a*) shows the variations of S_a^* as a function of y/h for PA_u and NA_u with $l_y^+ = 400$ in Re550. The shear parameter conditioned to NA_u is visibly larger than that of PA_u for $y/h > 0.02$. This suggests that NA_u originate under the strong shear conditions of the near-wall region, while PA_u are controlled by the low shear flow in the upper domain of the boundary layer. Moreover, the wall-normal variations of ET and LT of PA_u and NA_u with $l_y^+ = 400$ are displayed in figure 7(*b*). For PA_u, the values of ET and LT are closer to each other than those of NA_u when $y/h > 0.03$. Consequently, it can be hypothesised that the flow associated with NA_u is less likely to equilibrate during their life time to obey the logarithmic trends than that of PA_u, which is consistent with the asymmetrical features observed between PA_u and NA_u.

Finally, the trends for the inner peaks shown in figure 5 can also be interpreted from the sweep/ejection viewpoint. The inner peaks of PA_u arise from the top-to-bottom

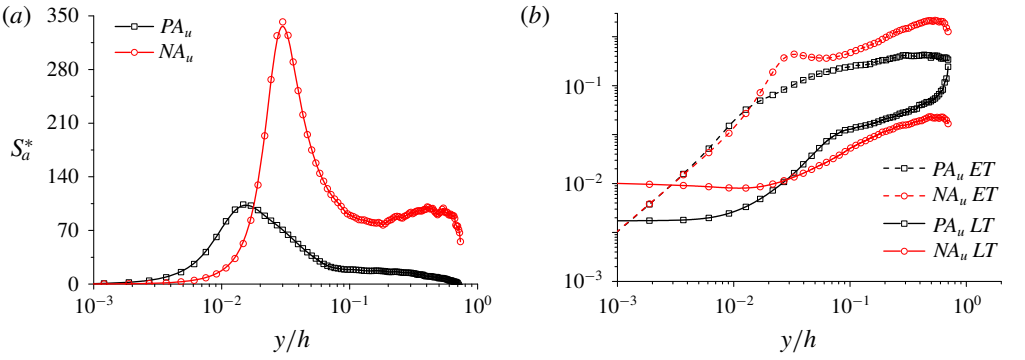

FIGURE 7. (*a*) Wall-normal variations of the conditional shear parameter (S_a^*) carried by PA_u and NA_u with $l_y^+ = 400$ in Re550. (*b*) Wall-normal variations of the life time and equilibration time of PA_u and NA_u with $l_y^+ = 400$ in Re550.

wall interactions of sweep events. In this context, it is reasonable to assume that the $\ln(Re_\tau)$ growth rate of the inner peak is mainly a consequence of the outer flow transported by PA_u.

3.2. *The wall-attached w-structures*

The spanwise fluctuating velocity represents another inactive component of the wall-attached eddies, which is also hypothesised to be geometrically self-similar. The length scales of wall-attached *w*-structures (PA_w and NA_w) are characterised by the joint p.d.f.s of l_x^+, l_z^+ with respect to l_y^+, which are shown in figure 8 using the case of Re550. Similarly to the observations for wall-attached *u*-structures, there is on average a nonlinear relationship between l_x^+ and l_y^+, whereas l_z^+ and l_y^+ are linearly proportional, both for PA_w and NA_w. The results support the geometrical self-similarity of wall-attached *w*-structures. The population densities of the wall-attached *w*-structures is displayed in figure 9. The densities decay as $n_d \propto (l_y^+)^{-1.6}$, similarly for PA_w and NA_w, unlike the trends obtained for *u*-structures. The geometrical and distributional features suggest no asymmetry between PA_w and NA_w, which is in line with expectations since the flow is statistically homogeneous in the spanwise direction. Moreover, one inevitable result of the symmetry, in stark contrast to the *u*-structures, is that the tendency of the *w*-structures associated with sweep and ejection events is absent. Figure 10 shows the joint p.d.f.s of w^+ and v^+ at $y/h = 0.2$ conditioned to PA_w and NA_w with $l_y^+ = 400$ in Re550. The p.d.f.s are approximately symmetrical along $v^+ = 0$, which suggests that PA_w and NA_w connect with the sweep and ejection events in the same manner, as expected.

Given the symmetries reported between PA_w and NA_w, the statistical moments of w are examined without distinguishing their signs. We define AA_w as $AA_w = PA_w + NA_w$ and follow the definition of $\langle u_a^{2p+}\rangle^{1/p}$ in (3.1). The conditional statistical moments of w, $\langle w_a^{2p+}\rangle^{1/p}$, are shown in figure 11(*a*). As l_y^+ increases, the moments of w tend to decay logarithmically. Figure 11(*b*) shows the corresponding indicator function Ξ to assess the logarithmic scaling. The values of Ξ are roughly constant in the range of $80 < y^+ < 160$, which indicates that the wall-attached *w*-structures behave similarly to ideal attached eddies. Nevertheless, the plateaus are less defined than those observed for *u*-structures. This phenomenon appears to contradict the observations

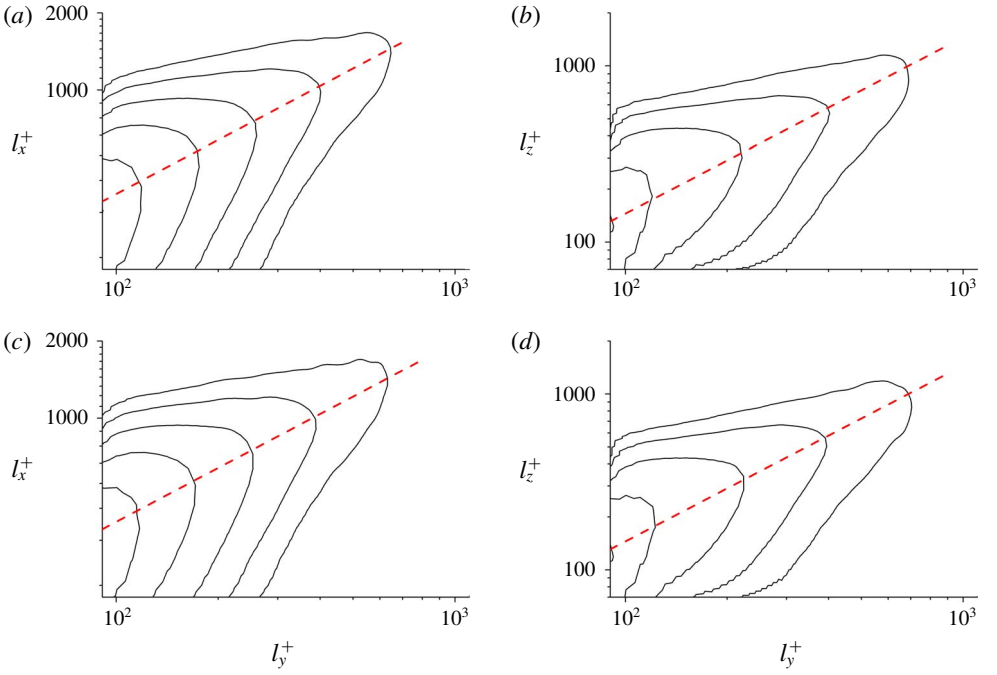

FIGURE 8. (*a*,*b*) Joint p.d.f.s of the length (l_x^+) and width (l_z^+) of PA_w in Re550 with respect to their height (l_y^+). The red dashed lines in (*a*,*b*) denote $l_x^+ = 15.65(l_y^+)^{0.70}$ and $l_z^+ = 1.45l_y^+$, respectively. (*c*,*d*) Joint p.d.f.s of the length (l_x^+) and width (l_z^+) of NA_w in Re550 with respect to their height (l_y^+). The red dashed lines in (*c*,*d*) denote $l_x^+ = 15.65(l_y^+)^{0.70}$ and $l_z^+ = 1.45l_y^+$, respectively. All of these p.d.f.s are logarithmically distributed.

of Lee & Moser (2015), who reported that the logarithmic decay of spanwise turbulence intensity is more robust than that of streamwise turbulence intensity. This is presumably caused by the inclusion of NA_u in the streamwise turbulence intensity. As an aside, the logarithmic scaling of AA_w is more notable as Re_τ increases, which will be reported in § 3.3.

3.3. *Reynolds-number effects on the statistical properties of the structures*

In this subsection, the other three cases (Re180, Re350 and Re950) are included to assess the Reynolds-number effects on the statistical properties of the wall-attached *u*- and *w*-structures.

3.3.1. *The wall-attached u-structures*

We first focus on the statistical properties of the wall-attached *u*-structures. As for the geometrical features, the relationships between l_x^+, l_z^+ and l_y^+ can be expressed as $l_x^+ \propto (l_y^+)^{\gamma_1}$ and $l_z^+ \propto (l_y^+)^{\gamma_2}$, respectively. Figure 12(*a*) shows the variations of γ_1 and γ_2 as a function of Re_τ. Note that only the structures with $l_y^+ > 100$ are taken into account. As Re_τ increases, γ_1 seems to converge to a constant value; whereas remarkable asymmetries are always observed between PA_u and NA_u, regardless of Re_τ. The value of γ_2 is in close proximity that when $Re_\tau \geqslant 547$, indicating the self-similarity of the *u*-structures. The population density of the structures is represented by $n_d \propto (l_y^+)^{-\gamma_3}$,

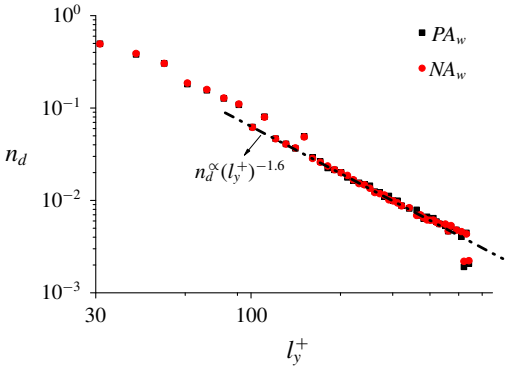

FIGURE 9. The population density (n_d) of PA_w and NA_w in Re550 as a function of l_y^+. The black dashed line represents $n_d \propto (l_y^+)^{-1.6}$.

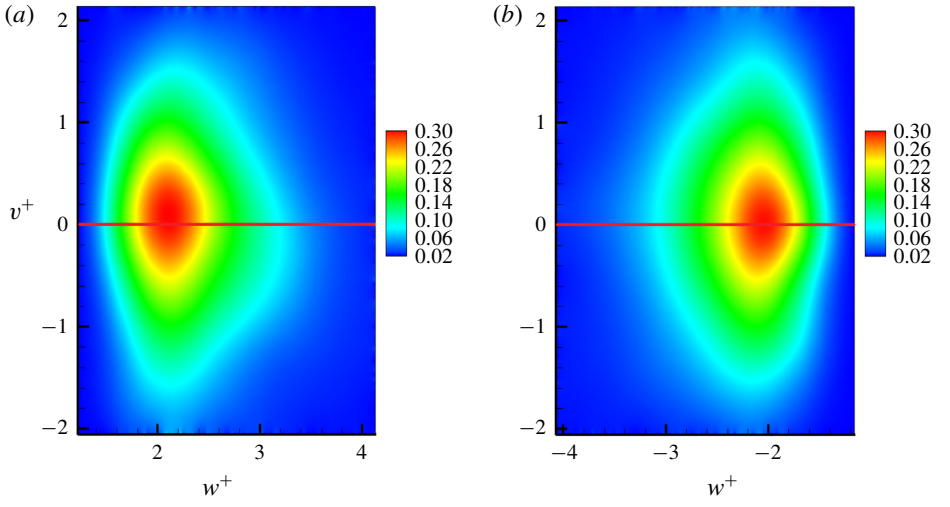

FIGURE 10. The joint p.d.f.s of w^+ and v^+ at $y/h = 0.2$ for PA_w (a) and NA_w (b) with $l_y^+ = 400$ in Re550. The red lines denote $v^+ = 0$.

and the variations of the index γ_3 are shown in figure 12(b) as a function of Re_τ. As seen, the values of γ_3 for PA_u are invariably close to the predictions of the attached-eddy model.

We next examine Reynolds-number effects on the statistical moments of the u-structures. Figure 13 shows the corresponding indicator function Ξ of the second-order moment of the u-structures for all cases. It can be seen that comparatively well-defined plateaus are observed for PA_u. The plateaus start from $y^+ \approx 80$, which corresponds to the lower limit of the logarithmic region (Jiménez 2018; Baars & Marusic 2020). For NA_u, however, Ξ does not approach a constant value. Note that the wrinkles in figure 13 may be caused by a lack of DNS samples. To the authors knowledge, this is the first time the logarithmic decay of the streamwise turbulence intensity at such low Reynolds numbers ($Re_\tau \approx 180$–550) has been shown.

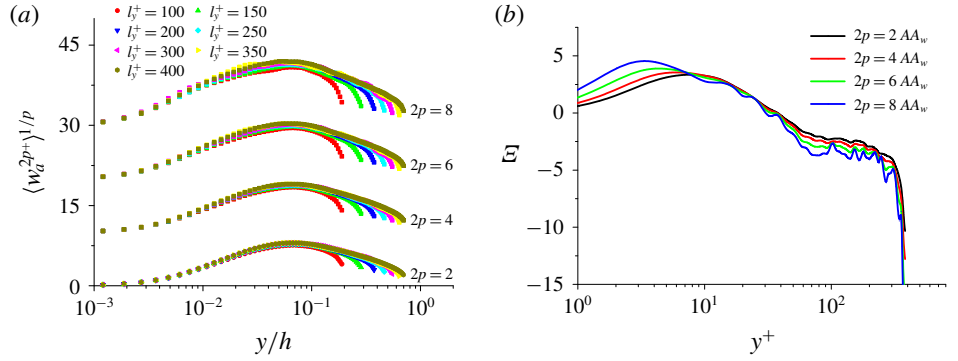

FIGURE 11. (*a*) Wall-normal variations of the 2*p*th root of the moments of the spanwise velocity fluctuations carried by AA_w with several selected wall-normal heights in Re550. The profiles of the 4th, 6th and 8th roots of moments are shifted upward by $\Delta\langle w_a^{4+}\rangle^{1/2} = 10$, $\Delta\langle w_a^{6+}\rangle^{1/3} = 20$ and $\Delta\langle w_a^{8+}\rangle^{1/4} = 30$, respectively. (*b*) Wall-normal variations of the corresponding indicator functions of the statistical moments from $2p = 2$ to $2p = 8$ for AA_w with $l_y^+ = 400$ in Re550.

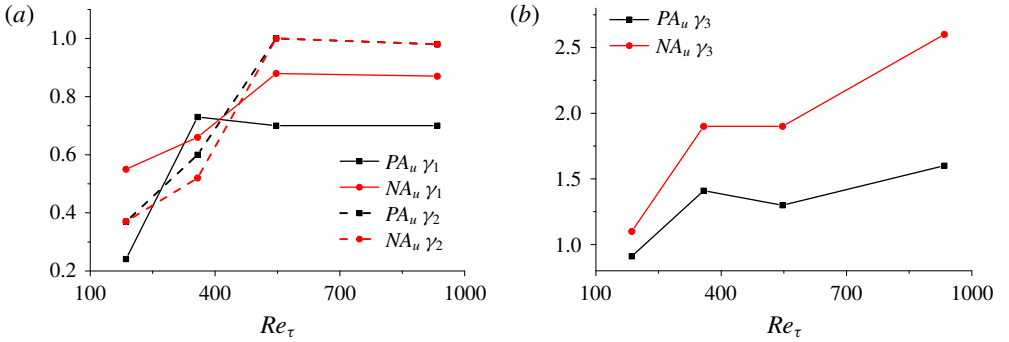

FIGURE 12. (*a*) The variations of γ_1 and γ_2 as a function of Re_τ for *u*-structures. (*b*) The variations of γ_3 as a function of Re_τ for *u*-structures.

Finally, the growth rates of the inner peaks associated with PA_u at different Reynolds number are examined and displayed in figure 14. The growth rates of the inner peaks are increased with the Reynolds number and tend to be consistent with the experimental results when $Re_\tau \geqslant 547$. The mismatches in Re180 and Re350 are probably related to the viscous effect, which plays a non-negligible role in outer flow transport.

3.3.2. *The wall-attached w-structures*

We examine the Reynolds-number effects on statistical properties of the wall-attached *w*-structures. Due to the lack of asymmetry between PA_w and NA_w, we only take AA_w ($AA_w = PA_w + NA_w$) into account. Figure 15 shows the variations of γ_1, γ_2 and γ_3 as functions of Re_τ for AA_w. As Re_τ increases, the values of γ_1 and γ_2 tend to be one, indicating the formation of the self-similarity. For γ_3, its value is not far from the theoretical prediction ($\gamma_3 = 1$), by and large.

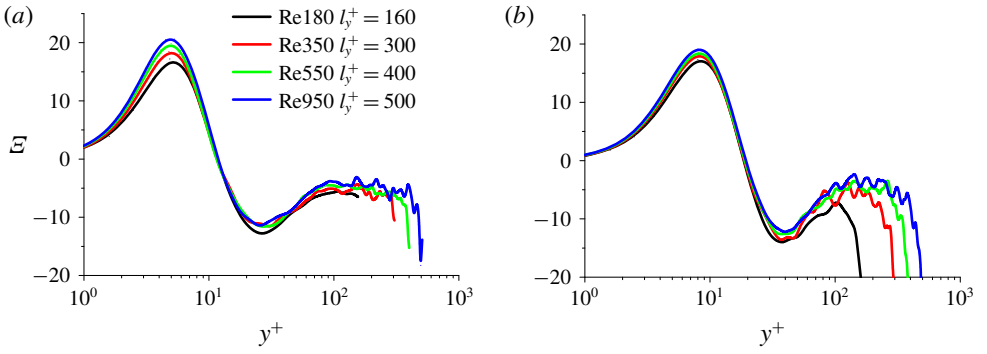

FIGURE 13. Wall-normal variations of the corresponding indicator function of the second-order moment for PA_u (*a*) and NA_u (*b*) with selected l_y^+ for all cases.

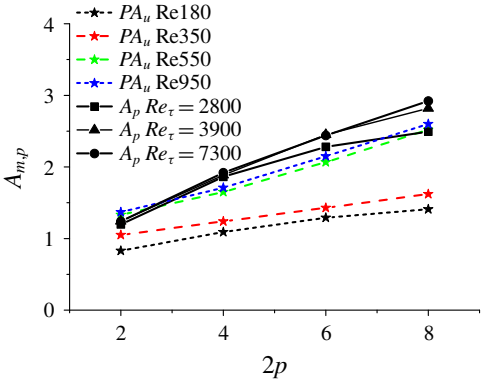

FIGURE 14. Variations of the growth rates of the inner peaks ($A_{m,p}$) associated with PA_u at different Reynolds numbers as a function of the moment order $2p$, compared with the A_p obtained from experiments (Meneveau & Marusic 2013).

To assess the logarithmic scaling of the spanwise turbulence intensity, figure 16 shows the corresponding indicator function Ξ of the second-order moment of the w-structures. It is readily noted that the plateau is observed in the range $80 < y^+ < 250$ in Re950. It would be hypothesised that the logarithmic scaling of spanwise turbulence intensity is more significant at higher Reynolds numbers.

4. Conclusions

In the present work, we adopted a three-dimensional clustering methodology to identify the wall-attached structures of streamwise and spanwise velocity fluctuations in turbulent channel flows at four Reynolds numbers ($Re_\tau = 186$, 358, 547 and 934). The structures are further classified into high- and low-speed families, denoted by *PA* and *NA*, respectively.

For the wall-attached u-structures, our results show that the statistical properties of PA_u and NA_u are asymmetrical, and the former exhibit a closer resemblance to the theoretical predictions of the attached-eddy model, namely, (i) the spanwise length scales are self-similar with the distance to the wall (y), (ii) the population

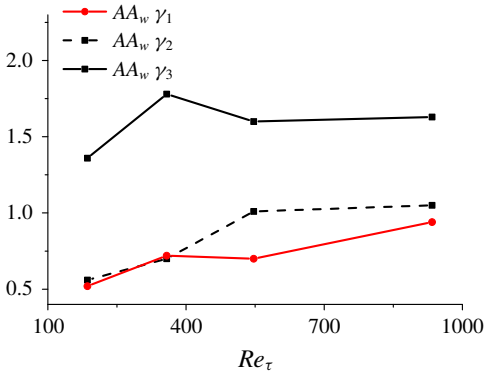

FIGURE 15. The variations of γ_1 , γ_2 and γ_3 as a function of Re_τ for AA_w.

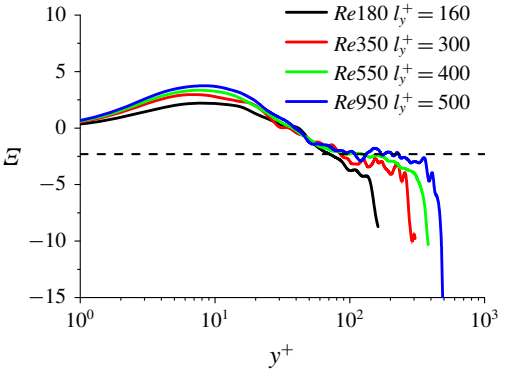

FIGURE 16. Wall-normal variations of the corresponding indicator function of the second-order moment for AA_w with selected l_y^+ for all cases.

density is inversely proportional to y, (iii) the statistical moments obey a logarithmic wall-normal scaling and (iv) the inner peaks of the statistical moments increase as $\ln(l_y^+)$. Although the low-Reynolds-number effect ($Re_\tau = 186$ and 358) obscures the geometric self-similarity, the logarithmic decay of the streamwise turbulence intensity carried by PA_u is still maintained. Furthermore, we have provided an interpretation of the asymmetric behaviour between PA_u and NA_u from the perspective of sweep and ejection events: PA_u are mostly associated with sweep events, while NA_u are strongly correlated with the ejection events. As a result, the formation of PA_u and NA_u are different due to the asymmetry introduced by the wall: PA_u are predominantly dominated by low shear flow from the upper domain of the boundary layer and NA_u originate under the strong shear conditions of the near-wall region. For the wall-attached w-structures, no asymmetry is found between the high- and low-speed families, and their statistical properties are approximately consistent with the predictions of Townsend's wall-attached model.

Note that the original attached-eddy model (Townsend 1976; Perry & Chong 1982) and subsequent variants (Woodcock & Marusic 2015; Yang, Marusic & Meneveau 2016) are incapable of describing the asymmetrical features of high- and

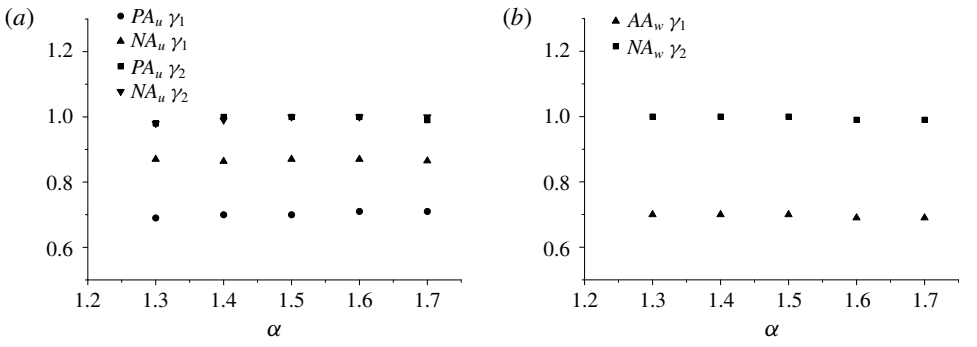

FIGURE 17. The variations of γ_1 and γ_2 as a function of α for (*a*) *u*-structures and (*b*) *w*-structures in Re550.

low-speed wall-attached *u*-structures. The presence of attached eddies in the low-Reynolds-number wall turbulence presented here may aid the development of future investigations of the attached-eddy model and allow for computationally efficient strategies for wall-bounded turbulence prediction.

Acknowledgements

This work was funded by the National Natural Science Foundation of China (under grant nos 11772194 and 91952302) and the Coturb program of the European Research Council, and performed in part during the fourth Madrid Turbulence Workshop at UPM. We would like to thank Professor Jiménez for his kind invitation to the workshop. We also express our gratitude to the reviewers of this paper for their kind and constructive comments.

Declaration of interests

The authors report no conflict of interest.

Appendix. Effects of the threshold α

The influence of the threshold α is examined. Figures 17(*a*) and 17(*b*) show the variations of γ_1 and γ_2 as a function of α for the *u*-structures and *w*-structures in Re550, respectively. The indices barely change when α varies from 1.3 to 1.7, indicating that the geometrical characteristics of the wall-attached structures are robust. Next, we examine the influence of α on the statistical moments. For PA_u, NA_u and AA_w, the indicator functions (Ξ) of the second-order moment over $1.3 \leqslant \alpha \leqslant 1.7$ are shown in figures 18(*a*), 18(*b*) and 18(*c*), respectively. The results suggest that the wall-normal scalings of the second-order moment are independent of α. The growth rates of the inner peaks of PA_u are plotted in figure 18(*d*) as a function of moment order $2p$ when α varies from 1.3 to 1.7, and compared with the data obtained from high-Reynolds-number experiments (Meneveau & Marusic 2013). It can be seen that the growth rates of PA_u do not change quantitatively within the range of α considered.

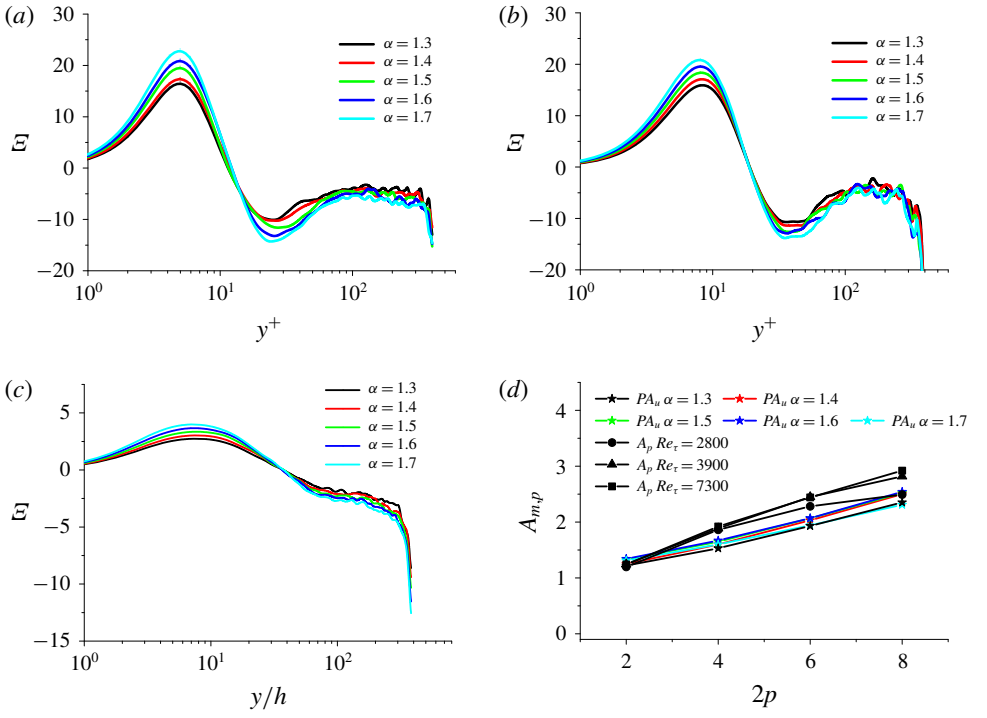

FIGURE 18. The indicator functions of the second-order moment carried by (*a*) PA_u, (*b*) NA_u and (*c*) AA_w with $l_y^+ = 400$ over $1.3 \leqslant \alpha \leqslant 1.7$ in Re550. (*d*) The growth rates of the inner peaks ($A_{m,p}$) of PA_u as a function of the moment order $2p$ when α varies from 1.3 to 1.7. The experimental measurements of A_p are also shown for comparison (Meneveau & Marusic 2013).

REFERENCES

AGOSTINI, L. & LESCHZINER, M. 2014 On the influence of outer large-scale structures on near-wall turbulence in channel flow. *Phys. Fluids* **26** (7), 075107.

AGOSTINI, L. & LESCHZINER, M. 2016*a* On the validity of the quasi-steady-turbulence hypothesis in representing the effects of large scales on small scales in boundary layers. *Phys. Fluids* **28** (4), 045102.

AGOSTINI, L. & LESCHZINER, M. 2016*b* Predicting the response of small-scale near-wall turbulence to large-scale outer motions. *Phys. Fluids* **28** (1), 339–352.

AGOSTINI, L. & LESCHZINER, M. 2019 The connection between the spectrum of turbulent scales and the skin-friction statistics in channel flow at $Re_\tau \approx 1000$. *J. Fluid Mech.* **871**, 22–51.

ALFREDSSON, P. H., SEGALINI, A. & ÖRLÜ, R. 2011 A new scaling for the streamwise turbulence intensity in wall-bounded turbulent flows and what it tells us about the outer peak. *Phys. Fluids* **23** (4), 041702.

BAARS, W. J., HUTCHINS, N. & MARUSIC, I. 2017 Self-similarity of wall-attached turbulence in boundary layers. *J. Fluid Mech.* **823**, R2.

BAARS, W. J. & MARUSIC, I. 2020 Data-driven decomposition of the streamwise turbulence kinetic energy in boundary layers. Part 2. Integrated energy and A_1. *J. Fluid Mech.* **882**, A26.

CHENG, C., LI, W., LOZANO-DURÁN, A. & LIU, H. 2019 Identity of attached eddies in turbulent channel flows with bidimensional empirical mode decomposition. *J. Fluid Mech.* **870**, 1037–1071.

CHUNG, D., MARUSIC, I., MONTY, J. P., VALLIKIVI, M. & SMITS, A. J. 2015 On the universality of inertial energy in the log layer of turbulent boundary layer and pipe flows. *Exp. Fluids* **56** (7), 141.

CORRSIN, S. 1958 Local isotropy in turbulent shear flow. *NACA Res. Memo.* 58B11.

DAVIDSON, P. A., NICKELS, T. B. & KROGSTAD, P.-Å. 2006 The logarithmic structure function law in wall-layer turbulence. *J. Fluid Mech.* **550**, 51–60.

DEL ÁLAMO, J. C., JIMÉNEZ, J., ZANDONADE, P. & MOSER, R. D. 2004 Scaling of the energy spectra of turbulent channels. *J. Fluid Mech.* **500**, 135–144.

DEL ÁLAMO, J. C., JIMÉNEZ, J., ZANDONADE, P. & MOSER, R. D. 2006 Self-similar vortex clusters in the turbulent logarithmic region. *J. Fluid Mech.* **561**, 329–358.

DESHPANDE, R., MONTY, J. P. & MARUSIC, I. 2019 Streamwise inclination angle of large wall-attached structures in turbulent boundary layers. *J. Fluid Mech.* **877**, R4.

DONG, S., LOZANO-DURÁN, A., SEKIMOTO, A. & JIMÉNEZ, J. 2017 Coherent structures in statistically stationary homogeneous shear turbulence. *J. Fluid Mech.* **816**, 167–208.

HELLSTRÖM, L. H. O., MARUSIC, I. & SMITS, A. J. 2016 Self-similarity of the large-scale motions in turbulent pipe flow. *J. Fluid Mech.* **792**, R1.

HOYAS, S. & JIMÉNEZ, J. 2006 Scaling of the velocity fluctuations in turbulent channels up to $Re_\tau = 2003$. *Phys. Fluids* **18** (1), 011702.

HU, R., YANG, X. I. A. & ZHENG, X. 2020 Wall-attached and wall-detached eddies in wall-bounded turbulent flows. *J. Fluid Mech.* **885**, A30.

HU, R. & ZHENG, X. 2018 Energy contributions by inner and outer motions in turbulent channel flows. *Phys. Rev. Fluids* **3** (8), 084607.

HULTMARK, M., VALLIKIVI, M., BAILEY, S. C. C. & SMITS, A. J. 2012 Turbulent pipe flow at extreme Reynolds numbers. *Phys. Rev. Lett.* **108** (9), 094501.

HWANG, J. & SUNG, H. J. 2018 Wall-attached structures of velocity fluctuations in a turbulent boundary layer. *J. Fluid Mech.* **856**, 958–983.

HWANG, J. & SUNG, H. J. 2019 Wall-attached clusters for the logarithmic velocity law in turbulent pipe flow. *Phys. Fluids* **31** (5), 055109.

HWANG, J. & SUNG, H. J. 2017 Influence of large-scale motions on the frictional drag in a turbulent boundary layer. *J. Fluid Mech.* **829**, 751–779.

HWANG, Y. 2015 Statistical structure of self-sustaining attached eddies in turbulent channel flow. *J. Fluid Mech.* **767**, 254–289.

HWANG, Y. & BENGANA, Y. 2016 Self-sustaining process of minimal attached eddies in turbulent channel flow. *J. Fluid Mech.* **795**, 708–738.

JIMÉNEZ, J. 2018 Coherent structures in wall-bounded turbulence. *J. Fluid Mech.* **842**, P1.

JIMÉNEZ, J. & HOYAS, S. 2008 Turbulent fluctuations above the buffer layer of wall-bounded flows. *J. Fluid Mech.* **611**, 215–236.

KLEWICKI, J., FIFE, P. & WEI, T. 2009 On the logarithmic mean profile. *J. Fluid Mech.* **638**, 73–93.

LEE, M. & MOSER, R. D. 2015 Direct numerical simulation of turbulent channel flow up to $Re_\tau \approx 5200$. *J. Fluid Mech.* **774**, 395–415.

LOZANO-DURÁN, A. & BAE, H. J. 2019 Characteristic scales of Townsend's wall-attached eddies. *J. Fluid Mech.* **868**, 698–725.

LOZANO-DURÁN, A. & BORRELL, G. 2016 Algorithm 964: an efficient algorithm to compute the genus of discrete surfaces and applications to turbulent flows. *ACM Trans. Math. Softw.* **42** (4), 34:1–34:19.

LOZANO-DURÁN, A., FLORES, O. & JIMÉNEZ, J. 2012 The three-dimensional structure of momentum transfer in turbulent channels. *J. Fluid Mech.* **694**, 100–130.

LOZANO-DURÁN, A. & JIMÉNEZ, J. 2014 Effect of the computational domain on direct simulations of turbulent channels up to $Re_\tau = 4200$. *Phys. Fluids* **26** (1), 011702.

LOZANO-DURÁN, A. & JIMÉNEZ, J. 2014 Time-resolved evolution of coherent structures in turbulent channels: characterization of eddies and cascades. *J. Fluid Mech.* **759**, 432–471.

MARUSIC, I., BAARS, W. J. & HUTCHINS, N. 2017 Scaling of the streamwise turbulence intensity in the context of inner–outer interactions in wall turbulence. *Phys. Rev. Fluids* **2** (10), 100502.

MARUSIC, I. & KUNKEL, G. J. 2003 Streamwise turbulence intensity formulation for flat-plate boundary layers. *Phys. Fluids* **15** (8), 2461–2464.

MARUSIC, I. & MONTY, J. P. 2019 Attached eddy model of wall turbulence. *Annu. Rev. Fluid Mech.* **51**, 49–74.

MARUSIC, I., MONTY, J. P., HULTMARK, M. & SMITS, A. J. 2013 On the logarithmic region in wall turbulence. *J. Fluid Mech.* **716**, R3.

MATHIS, R., MARUSIC, I., CHERNYSHENKO, S. I. & HUTCHINS, N. 2013 Estimating wall-shear-stress fluctuations given an outer region input. *J. Fluid Mech.* **715**, 163–180.

MEHREZ, A., PHILIP, J., YAMAMOTO, Y. & TSUJI, Y. 2019 Pressure and spanwise velocity fluctuations in turbulent channel flows: logarithmic behavior of moments and coherent structures. *Phys. Rev. Fluids* **4** (4), 044601.

MENEVEAU, C. & MARUSIC, I. 2013 Generalized logarithmic law for high-order moments in turbulent boundary layers. *J. Fluid Mech.* **719**, R11.

MIZUNO, Y. & JIMÉNEZ, J. 2011 Mean velocity and length-scales in the overlap region of wall-bounded turbulent flows. *Phys. Fluids* **23** (8), 085112.

MOISY, F. & JIMÉNEZ, J. 2004 Geometry and clustering of intense structures in isotropic turbulence. *J. Fluid Mech.* **513**, 111–133.

MOURI, H. 2017 Two-point correlation in wall turbulence according to the attached-eddy hypothesis. *J. Fluid Mech.* **821**, 343–357.

OSAWA, K. & JIMÉNEZ, J. 2018 Intense structures of different momentum fluxes in turbulent channels. *Phys. Rev. Fluids* **3**, 084603.

PERRY, A. & MARUSIC, I. 1995 A wall-wake model for the turbulence structure of boundary layers. Part 1. Extension of the attached eddy hypothesis. *J. Fluid Mech.* **298**, 361–388.

PERRY, A. E. & CHONG, M. S. 1982 On the mechanism of wall turbulence. *J. Fluid Mech.* **119** (119), 173–217.

PERRY, A. E., HENBEST, S. & CHONG, M. S. 1986 A theoretical and experimental study of wall turbulence. *J. Fluid Mech.* **165**, 163–199.

SILLERO, J. A., JIMÉNEZ, J. & MOSER, R. D. 2013 One-point statistics for turbulent wall-bounded flows at Reynolds numbers up to $\delta^+ \approx 2000$. *Phys. Fluids* **25** (10), 105102.

TOWNSEND, A. A. 1976 *The Structure of Turbulent Shear Flow*, 2nd edn. Cambridge University Press.

WALLACE, J. M. 2016 Quadrant analysis in turbulence research: history and evolution. *Annu. Rev. Fluid Mech.* **48**, 131–158.

WANG, W., PAN, C. & WANG, J. 2018 Quasi-bivariate variational mode decomposition as a tool of scale analysis in wall-bounded turbulence. *Exp. Fluids* **59** (1), 1.

WANG, W., PAN, C. & WANG, J. 2019 Multi-component variational mode decomposition and its application on wall-bounded turbulence. *Exp. Fluids* **60** (6), 95.

WOODCOCK, J. D. & MARUSIC, I. 2015 The statistical behaviour of attached eddies. *Phys. Fluids* **27** (1), 97–120.

YAMAMOTO, Y. & TSUJI, Y. 2018 Numerical evidence of logarithmic regions in channel flow at $Re_\tau = 8000$. *Phys. Rev. Fluids* **3** (1), 012602.

YANG, Q., WILLIS, A. P. & HWANG, Y. 2019 Exact coherent states of attached eddies in channel flow. *J. Fluid Mech.* **862**, 1029–1059.

YANG, X., BAIDYA, R., LV, Y. & MARUSIC, I. 2018 Hierarchical random additive model for the spanwise and wall-normal velocities in wall-bounded flows at high Reynolds numbers. *Phys. Rev. Fluids* **3** (12), 124606.

YANG, X. I. A., MARUSIC, I. & MENEVEAU, C. 2016 Moment generating functions and scaling laws in the inertial layer of turbulent wall-bounded flows. *J. Fluid Mech.* **791**, R2.

YOON, M., HWANG, J., YANG, J. & SUNG, H. J. 2020 Wall-attached structures of streamwise velocity fluctuations in an adverse-pressure-gradient turbulent boundary layer. *J. Fluid Mech.* **885**, A12.